2-15-2024

Numerical investigation of the thermo-hydraulic performance of a shark denticle-inspired plate fin heat exchanger

Aakash S. Hurry
Edith Cowan University

Ana Vafadar
Edith Cowan University

Kevin Hayward
Edith Cowan University

Ferdinando Guzzomi
Edith Cowan University

Kanishk Rauthan
Edith Cowan University

10.1016/j.applthermaleng.2023.122192
Hurry, A. S., Vafadar, A., Hayward, K., Guzzomi, F., & Rauthan, K. (2024). Numerical investigation of the thermo-hydraulic performance of a shark denticle-inspired plate fin heat exchanger. Applied Thermal Engineering, 239, article 122192. https://doi.org/10.1016/j.applthermaleng.2023.122192

Applied Thermal Engineering 239 (2024) 122192

Contents lists available at ScienceDirect

Applied Thermal Engineering

journal homepage: www.elsevier.com/locate/apthermeng

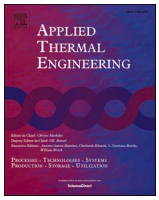

Research Paper

Numerical investigation of the thermo-hydraulic performance of a shark denticle-inspired plate fin heat exchanger

Aakash S. Hurry [a,1,*], Ana Vafadar [b,1], Kevin Hayward [c,1], Ferdinando Guzzomi [c,1], Kanishk Rauthan [d,1]

[a] PhD Research Candidate in Mechanical Engineering, School of Engineering, Edith Cowan University (ECU), Australia
[b] Lecturer, School of Engineering, Edith Cowan University (ECU), Postal address: JO5.224, 270 Joondalup Drive, Joondalup, WA 6027, Australia
[c] Senior Lecturer, School of Engineering, Edith Cowan University (ECU), Australia
[d] Master by Research Graduate, School of Engineering, Edith Cowan University (ECU), Postal address: JO27.303, 270 Joondalup Drive, Joondalup, WA 6027, Australia

ARTICLE INFO

Keywords:
Plate fin heat exchanger
Biomimicry
Heat exchanger design
Reverse engineering
Thermo-hydraulic performance
Numerical analysis

ABSTRACT

Growing demand for increased power dissipation is fuelling the need for the design of more efficient heat exchangers. Modifying fin geometry is an effective way of improving heat transfer efficiency and of reducing flow resistance for plate fin heat exchangers. To date, fin designs have mostly revolved around classical shapes such as pins, ellipses, and rectangles, due to limitations of conventional manufacturing technologies. However, with recent advancements in metal additive manufacturing, there is an opportunity of redesigning approaches and ways of thinking to create novel fin geometries. In this study, biomimicry was used as a tool to reverse engineer a novel geometry for a plate fin heat exchanger based on a denticle, which is a mesoscopic structure on the skin of sharks. The shape of the denticle is streamlined; therefore, showing the possibility of enhancing fluid-to-solid contact if used as geometry for a plate fin heat exchanger. The thermo-hydraulic performance of the denticle was evaluated with respect to a rectangular, cylindrical and an elliptical fin (NACA 0030), using conjugate-heat-transfer simulations on ANSYS-Fluent. The numerical model was calibrated and validated based on experimental results from an additively manufactured rectangular plate fin heat exchanger. Results demonstrated that over the range of tested Reynolds Numbers, $9.8x10^4 < Re \leq 22.9x10^4$, the denticle fin had average Nusselt number improvements of 13.1 %, 5.4 % and 75.7 % with respect to the rectangular fin, the NACA 0030 and cylindrical fin, respectively. At $Re = 22.9x10^4$, a 26 % decrease in pressure drop was noted for the denticle with respect to the rectangular fin, with maximum thermal performance factors (η) of 1.29, 0.81 and 1.53 as noted for the denticle fin with respect to the rectangular fin, NACA 0030 fin and cylindrical fin, respectively.

1. Introduction

Heat Exchangers (HXs) are crucial for a variety of applications, such as in electronic devices, turbines and power plants, where adequate heat transfer is required to preserve product reliability and operational capabilities [1]. HXs can be classified based on their flow path, heat transfer process and by construction type [2–4]. Most conventionally manufactured HXs consist of primary heat transfer surfaces such as plates, sheets and circular tubes, all of which restrain thermal and pressure drop performances [5]. Plate fin HXs (PFHXs) are widely used because of their abilities to enhance thermal, and pressure drop performance as compared to conventional plate HXs [6,7]. Whilst PHFXs have higher efficiencies, variations in their fin geometries can affect heat transmission and resistance to fluid flow [8–11]. Accordingly, pressure drop can outweigh thermal performance enhancement. An increase in pressure drop usually leads to higher pumping requirements [12]. Hence, a trade-off between thermal enhancement and pressure drop is required when designing fins for HXs [13].

Advancements of Additive Manufacturing (AM) technologies in printing metal parts provides an unprecedented degree of freedom in the design and manufacturing of HXs with novel fin geometries [14]. Fin geometry facilitates heat transmission and fluid flow in order to boost overall heat transfer efficiency and to reduce flow resistance [8–11].

* Corresponding author.
E-mail addresses: ahurry@our.ecu.edu.au (A.S. Hurry), a.vafadar@ecu.edu.au (A. Vafadar), Kevin.Hayward@ecu.edu.au (K. Hayward), f.guzzomi@ecu.edu.au (F. Guzzomi), k.rauthan@ecu.edu.au (K. Rauthan).
[1] JO5.238, 270 Joondalup Drive, Joondalup WA 6027, Australia.

https://doi.org/10.1016/j.applthermaleng.2023.122192
Received 3 January 2023; Received in revised form 4 August 2023; Accepted 7 December 2023
Available online 10 December 2023

Nomenclature

A_{fb}	fin base contact surface area [mm^2]
$A_{fin\ wall}$	extended fin wall surface area [mm^2]
$A_{frontal}$	frontal area [mm^2]
D_h	hydraulic diameter [m]
D_ω	cross-diffusion term
F_2	blending function
f	friction factor
G_k	production of turbulent kinetic energy
G_{kb}	buoyancy term for turbulent kinetic energy
G_ω	generation of dissipation rate
$G_{\omega b}$	buoyancy term for dissipation rate
h	enthalpy [J/kg]
h_c	heat transfer coefficient [W/m^2K]
H	height of test section [m]
$\vec{J}_j$	diffusion of flux species j
k	thermal conductivity [W/mK]
k_{eff}	effective thermal conductivity [W/mK]
L	length between pitot tubes [m]
L_f	characteristic length of fin [m]
m	mass [g]
Nu	Nusselt number
$P_{gauge,\ outlet}$	outlet gauge pressure [Pa]
ΔP	pressure drop [Pa]
$\Delta P_{Exp.}$	experimental pressure drop [Pa]
ΔP_{diff}	difference between experimental and simulation pressure drop [Pa]
$\Delta P_{Sim.}$	simulation pressure drop [Pa]
$q_{out,k}$	energy flux [W/m^2]
Q“	heat flux [W/m^2]
Re	Reynolds number
S	strain rate magnitude
S_k	user defined source term for turbulent kinetic energy
S_ω	user defined source term for dissipation rate
T	temperature [K]
T_{atm}	atmospheric air temperature [°C]
$T_{fin\ surf.}$	fin surface temperature [°C]
$T_{fin\ surf.\ Exp}$	experimental fin surface temperature [°C]
$T_{fin\ surf.\ Sim}$	simulation fin surface temperature [°C]
T_{inlet}	inlet air temperature [°C]
$T_{fin\ surf.\ Sim}$	simulation fin surface temperature [°C]
T_{inlet}	inlet air temperature [°C]
T_k	surface temperature [K]
T_{outlet}	outlet air temperature [°C]
ΔT_{diff}	difference between experimental and simulation fin surface temperature [°C]
u_i	velocity component [m/s]
u	velocity [m/s]
$\vec{u}$	overall velocity vector [m/s]
W	width of test section [m]
Y_k	dissipation of turbulent kinetic energy due to turbulence
Y_ω	dissipation rate due to turbulence
y	distance to next surface [m]
y^+	non dimensional length scale for turbulence

Greek Letters

σ	Stefan-Boltzmann constant [W/m^2K^4]
σ_k	turbulent Prandtl number for kinetic energy
σ_ω	turbulent Prandtl number for dissipation rate
ε_k	surface emissivity
ρ	fluid density [kg/m^3]
μ	dynamic viscosity [Pa·s]
μ_t	turbulent viscosity [Pa·s]
η	thermal performance factor
$\bar{\bar{\tau}}_{eff}$	effective stress tensor [Pa]
F_K	effective diffusivity of turbulent kinetic energy
F_w	effective diffusivity of dissipation rate

Abbreviations

AM	Additive Manufacturing
PFHX	Plate fin Heat Exchanger
HX	Heat Exchanger
SEM	Scanning Electron Microscopic
CHT	Conjugate Heat Transfer
S2S	Surface to Surface
SST	Shear-Stress Transport

However, despite the degree of freedom that is afforded by metal AM, there has been limited investigation up to now on designing PFHXs with innovative geometries [15]. To date, fin designs have mostly revolved around classical shapes such as pins, ellipses and rectangles [16–19]. In the field of thermal management, nature has seldom been used as a source of inspiration to develop more efficient HXs [20]. Only few biomimicry HXs have been designed that are recognised as final products of biomimicry [21].

A thorough literature review on nature-inspired heat exchangers can be found in [21]. Accordingly, biomimicry HX designs have thus far been limited to the following seven nature phenomena: leaf vein structure, leaf surface wettability, sweat glands system, lung and blood vein structures, counter current veins in penguin feet, fish body shapes and hummingbird wings [21]. The limited application of biomimicry in novel heat exchanger design might be attributed to an unawareness of its process, in addition to the complexity in identifying, extracting and applying information from nature across varied applications.

“ISO18458:2015 – Biomimetics – Terminology, concepts and Methodology” [22] describes how research surrounding biomimicry revolves around two processes: biology-push and technology-pull. Biology-push, also referred to as the bottom-up approach, involves analysing a discovery in terms of biology, extracting concepts and then applying these to technology. In contrast, technology-pull, equivalently termed as the top-down approach, consists of solving a problem using technology by looking at biology for plausible solutions [23]. For instance, technology-pull has mostly been used to remediate to problems in engineering applications. The inclusion of numerical simulations at early stages of the biomimicry design process helps provide better understanding, and in visualising flow patterns before proceeding with manufacturing of HXs [21].

Cui et al. [24] have used a combination of numerical and experimental approaches to develop an innovative skin for perspiration cooling by mimicking the thermoregulation mechanism in living organisms. Their results demonstrated improvements of up to twenty times in passive cooling performance [24]. Wang et al. [25] have expanded on the concept of the vein structure in leaves to develop an asymmetrical fractal HX, with their numerical results showing negligible thermal and pressure drop improvements at low branching numbers, but with significant improvements with higher branching numbers [25]. Additionally, Bacelar et al. [26] have used a combination of experimental and numerical studies to investigate the effect of a micro channel heat exchanger inspired by the fish body shape. Reductions of 10 % temperature and 20 % pumping power were noted for the bio-inspired design compared to a baseline micro channel heat exchanger. Likewise Gürel et.al [27] evaluated the thermo-hydraulic performance of a compact brazed plate HX embedded with a 3D lung pattern by using a

combination of experimental and numerical methods. Their numerical simulations were validated based on the experimental results of an existing chevron type compact brazed plate heat exchanger. Further, their results showed a 71 % increase in heat transfer and 6 % reduction in pressure drop respectively, for the biomimicry heat exchanger. Additionally, the use of numerical simulations was shown to aid visualisation of regions of high turbulence on the lung inspired heat exchanger.

By considering these previous investigations, the following can be noted: using nature as a source of inspiration has the potential of creating more efficient heat exchangers; and, a combination of both experimental and numerical approaches can be useful when developing novel nature-inspired heat exchangers. Likewise, for the development of more efficient PFHXs, effective aerodynamics, hydrodynamics and heat transfer strategies can be inspired from adaptations found in nature. For instance, the Shortfin Mako Shark is amongst the fastest aquatic animals, possessing external body adaptations for enhanced hydrodynamics ranging from the macroscopic to the mesoscopic scale [28]. This study aims to develop a novel fin geometry for a PFHX based on a denticle, which is a body adaptation of the Shortfin Mako Shark at the mesoscopic scale, as illustrated in Fig. 1(a). To evaluate the efficiency of the denticle PFHX, Conjugate Heat Transfer simulations (CHT) were performed using ANSYS Fluent. Numerical results were then used to analyse the thermo-hydraulic performance of the denticle PFHX with respect to commonly used geometries such as a rectangular PFHX, an airfoil (NACA 0030) PFHX,and a cylindrical PFHX.

2. Methodology

2.1. Overview of the fin design

The following assumptions were made regarding the suitability of using a shark denticle as a fin for a PFHX:

- The morphology of the denticle is streamlined and effective in reducing drag, thereby showing the possibility of reducing boundary layer separation, which can be beneficial for enhanced heat transfer and reduced pressure drop.
- The stem of the denticle can serve as a base for heat extraction from the primary heat transfer surface of the HX (plate) and mimic the actual function of a fin in a PFHX.
- The presence of ridges on the denticle's upper surface can further increase streamlining by channelling fluid flow over the top surface, thereby improving the area of contact between the top of the fin and the flowing fluid for enhanced heat transfer.

Fig. 1 shows the overview of the biomimicry design process. The shark denticle-inspired fin HX, as shown in Fig. 1(a), was designed by using reconstructed views from a Scanning Electron Microscopic (SEM) image of a denticle, as illustrated in Fig. 1(b). Through reverse engineering, the shark denticle-inspired PFHX was designed on SolidWorks, as illustrated in Fig. 1(c). To evaluate the thermal performance of the denticle PFHX, three PFHXs with commonly used fin geometries were also included in this study as illustrated in Table 1. To normalise the effect of heat transfer by conduction, the following criteria were set as design constraints for the PFHXs: overall mass and fin base contact area, as listed in Table 1; and the use of Stainless Steel 17-4PH as material. A similar approach has been adopted by Vafadar et.al.[9] and Rauthan et al.[30] to investigate the pressure drop and/or heat transfer of single finned PFHXs. The fin base contact area is the area between the square base and extended part of the fin, while the frontal area corresponds to the area exposed to the fluid in the flow direction. The resultant surface area for heat transfer by convection and radiation for each PFHX is represented by the extended fin wall surface area ($A_{fin\ wall.}$), as illustrated in Table 1.

2.2. Overview of the study

In this work, the main target of the experimental section was to record measurements for pressure drop, heat flux and surface temperature for a baseline rectangular PFHX, and to use these results to validate a numerical model for conjugate heat transfer simulations on ANSYS

Table 1
Properties of PFHXs.

Geometry	Overall Mass, m (g)	Fin Base Contact Surface Area, $A_{fb.}$ (mm^2)	Extended fin wall surface area, $A_{fin\ wall.}$ (mm^2)	Frontal Area, $A_{frontal.}$ (mm^2)
Rectangular 	261	500	5900	450
Denticle 	261	500	4950	1130
NACA 0030 	261	500	5340	670
Cylindrical 	261	500	4060	1130

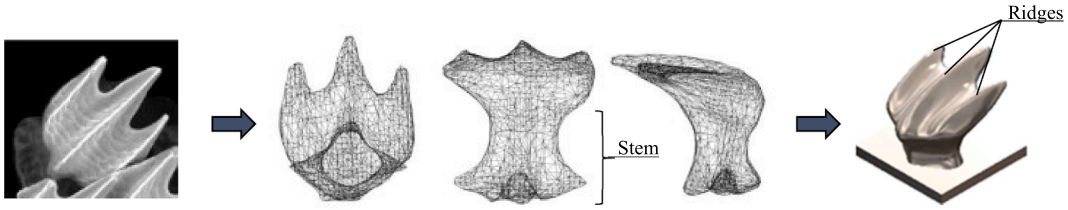

Fig. 1. Overview of biomimicry design process: (a) SEM of Shark Denticle [29]; (b) Views from a reconstructed micro-CT scan of a denticle [29]; and (c) Designed shark denticle-inspired PFHX.

Fluent. Once validated, the same numerical model was used to perform simulations on the remaining PFHXs. Thermal performance factor, η, was used to compare the relative overall thermo-hydraulic performance of the denticle PFHX with respect to the rectangular PFHX, NACA 0030 PFHX, and the cylindrical PFHX, respectively [31]. The rectangular PFHX was additively manufactured by using the Markforged Metal X printer through the AM process of bound powder extrusion [32]. The extended part (fin) of the rectangular PFHX measured 50 mm x 5 mm in length and breadth, and had a height of 45 mm. For the experimental study, a wind tunnel with a test section of 125 mm × 125 mm in breadth and height, and length of 350 mm was used to test the PFHX. The walls of the test section were made up of acrylic. The extended part of the PFHX was on the airside and the square base was on the solid side. The rectangular PFHX was centrally placed across the bottom panel of the test section. The top face of the base was flush with the acrylic panel. This ensured that only the effect of the extended surface was captured.

2.3. Experimental analysis

2.3.1. Experimental set-up

Experiments were conducted in a temperature controlled facility by using a "TecQuipment AF1125 Subsonic Wind Tunnel" [33], as shown in Fig. 2. Air can be drawn in the wind tunnel by means of a variable-speed fan, up to a speed of 30 m/s. The wind tunnel consists of a rectangular test section and is fitted with a honeycomb flow straightener at the inlet, which contributes to reducing lateral velocity and turbulence of incoming air. Air velocity was measured at the entrance of the test section by a hot-wire anemometer, and was controlled by using a variable speed controller. To ensure that heat transfer and pressure drop characteristics of the PFHX were not influenced by the presence of extra sensors in the flow field, experiments for each phenomenon were done separately.

For pressure drop measurements, a hot-wire anemometer probe was used to measure velocity, where pitot tubes and static pressure ports were used to measure inlet and outlet pressures. The pitot tubes were aligned centrally (z = 0) along the flow field, while the velocimeter probe was placed offset (z = -14 mm) to prevent hindering flow to the pitot tube. Relative to the inlet of the test section, the inlet and outlet pitot tubes were located at a length of 45 mm and 250 mm, respectively. Relative to the bottom acrylic panel, the inlet and outlet pitot tubes were located at a height of 105 mm and 22.5 mm, respectively. A plastic holder centrally positioned the PFHX along the bottom of the test section. Two digital pressure manometers were used to measure inlet and outlet differential pressures, as shown in Fig. 3(a).

For thermal performance measurements, a four-inch FLIR infrared glass [34] was retrofitted to an acrylic panel, as shown in Fig. 3(b). Matte black vinyl was placed on front, top and back acrylic panels to reduce environmental glare and reflection. For consistency, the hot-wire anemometer probe was placed at the same location on the top acrylic panel for pressure drop measurements. To support the PFHX in the test section, a copper block was machined and placed on top of a plate heater. A heat flux sensor and a RTD surface sensor were placed between the copper block and the PFHX. High thermal conductivity thermal paste was used at contact regions between PFHX, heat flux sensor, copper block and plate heater. To measure atmospheric temperature and inlet air temperature, two RTD probes were installed at the inlet of the wind tunnel and at the inlet of the test section, respectively. All temperature readings were captured by means of a data logger. Further, plastic fittings were printed and used to accommodate for temperature probes and seal unused pressure ports.

To minimise heat losses during thermal experiments, layers of insulation were applied to the copper block underneath the test section. This insulation consisted of two layers of calcium-magnesium silicate blanket interposed under one layer of ceramic and aluminium blanket and wrapped using silicone insulation tape. To minimise heat transfer to the bottom acrylic panel, a recessed calcium silicate cut-out was fixed at

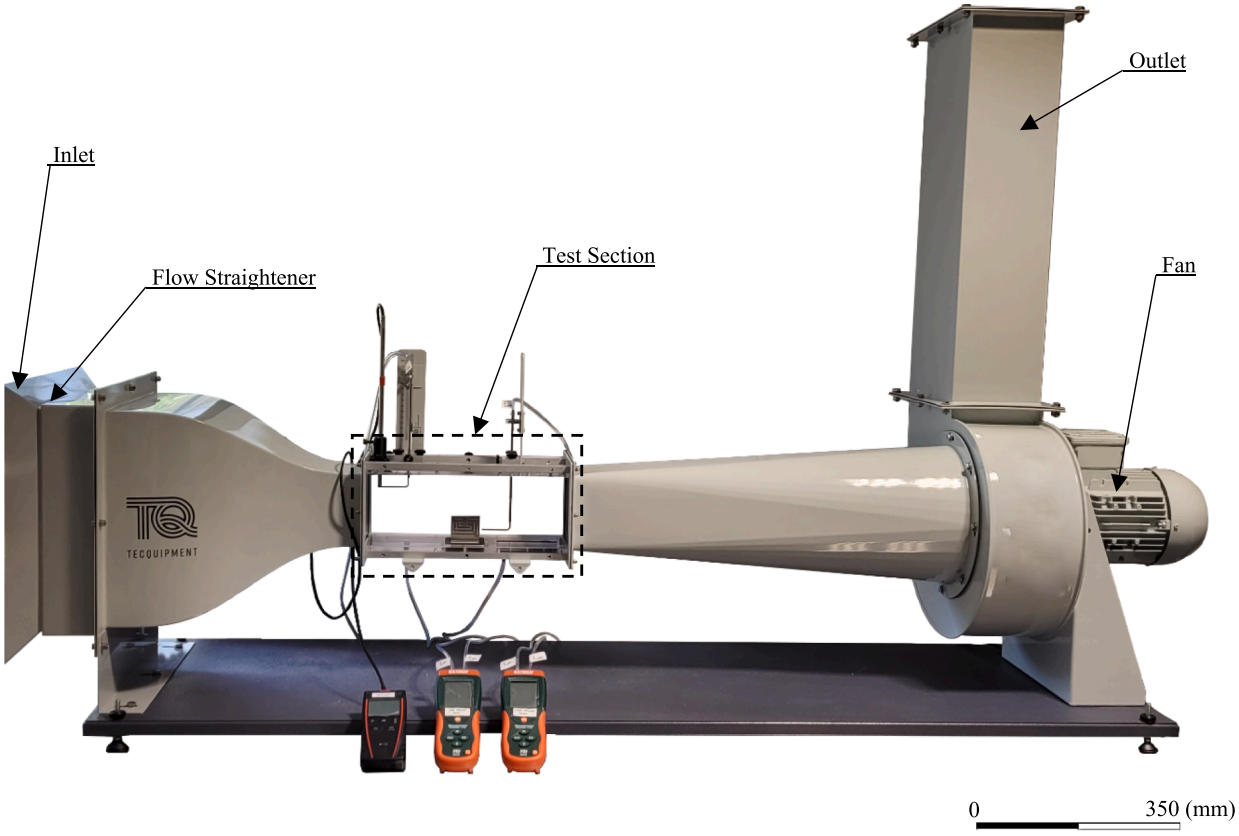

Fig. 2. Illustration of modified AF1125 subsonic wind tunnel for pressure measurement [54].

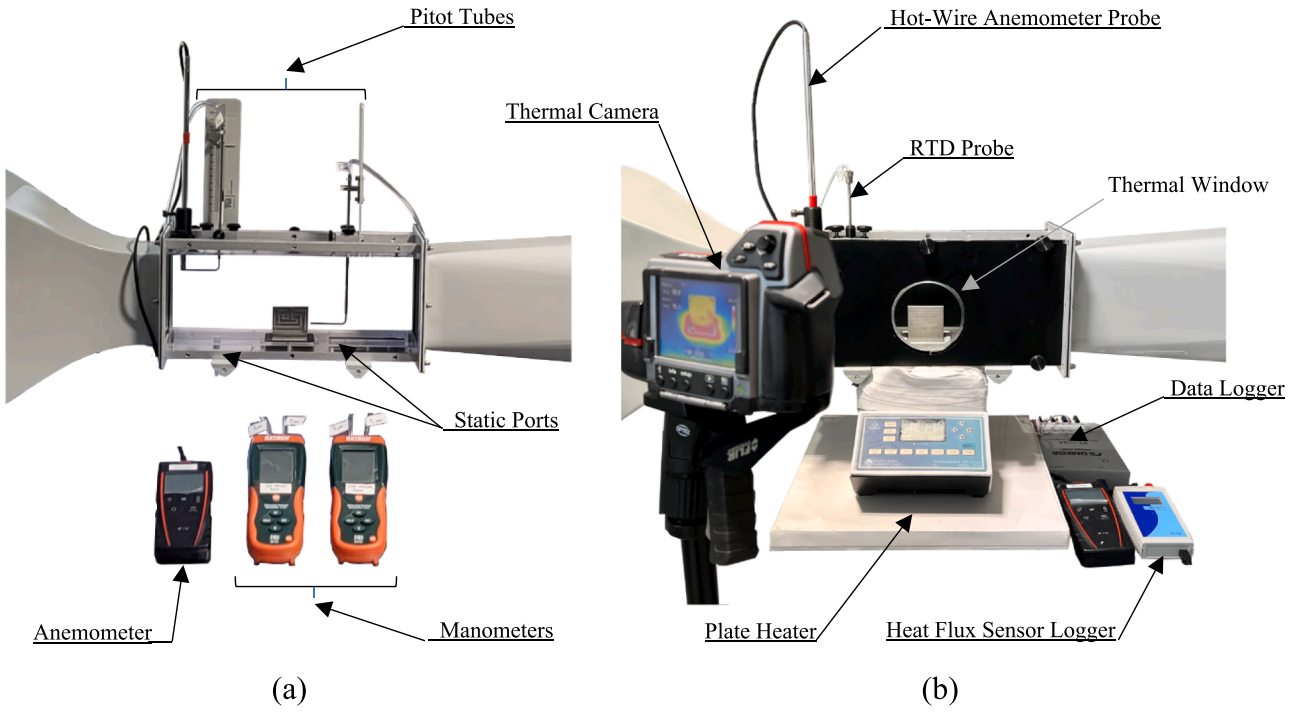

Fig. 3. Close up of test section for: (a) pressure drop measurements; & (b) heat transfer measurements [54].

the centre of the panel around the PFHX and the copper block. Further, the heater temperature was set at 80 °C to protect the integrity of acrylic panels over extensive testing periods.

For both thermal and pressure drop experiments, a KIMO VT110 hot-wire anemometer [35] with an accuracy of ± 0.1 m/s and a range of 0.15 m/s-30 m/s was used to measure the velocity, ν, at the inlet of the test section. To characterise the pressure drop between inlet and outlet pitot tubes, two Extech HD755 differential pressure manometers [36], each with an accuracy of ± 10 Pa and a range of 0–3000 Pa, were used. The rolling averages of velocity and pressure were taken for each experimental run, as both manometers and the anemometer could not be connected to data acquisition systems.

For thermal experiments, four RTD sensors with an accuracy of ± 0.01 °C were used to measure the temperature at different locations. Temperature data acquisition was measured through an Omega Pt-104a system [37] at a frequency of 0.0167 Hz. Heat flux was measured at the base of the PFHX by an FHF-04SC Hukseflux heat flux sensor [38], and logged using a Li-19 Hukseflux datalogger [39] with an accuracy of ± 10 W/m^2 at a frequency of 0.0167 Hz. The surface temperature of the rectangular fin was measured by a FLIR T200 [40] thermographic camera set in the range of 0 °C-120 °C with an accuracy of ± 2 °C. The camera has an infrared image resolution of 240x180 pixels. The emissivity of the PFHX was measured using surface RTD sensors.

2.3.2. *Experimental procedure and uncertainties*

Measurements of differential pressure, heat flux, atmospheric temperature and fin surface temperature were used to characterise thermal, and pressure drop performances of the rectangular PFHX. For pressure experiments, rolling averages for pressure and velocity readings were noted during each run. For $\nu \leq 10$ m/s, outlet pressure readings were too close or beyond the lower limit of the Extech HD755 differential pressure manometer and at $\nu = 30$ m/s, velocity readings were limited by the upper range of the KIMO VT110 hot-wire anemometer. Hence, due to these range limitations, experiments were performed at 4 m/s intervals between 12 m/s and 28 m/s.

For thermal performance analysis, pilot tests were performed to determine stable states for the rectangular PFHX prior to start and end experiments with the heater set at 80 °C throughout the tests. A stable state refers to a period during which the heat flux and the average surface temperature of the fin is relatively constant. Plots for heat flux and fin surface temperatures for the rectangular PFHX is shown in Fig. 4. For each thermal experimental run, readings for temperatures and heat flux were noted at 1 min intervals before and after the fin reached a stable state (between t = 0 min to t = 5 min, and t = 30 min to t = 35 min).

Experimental uncertainties [41] were calculated based on standard

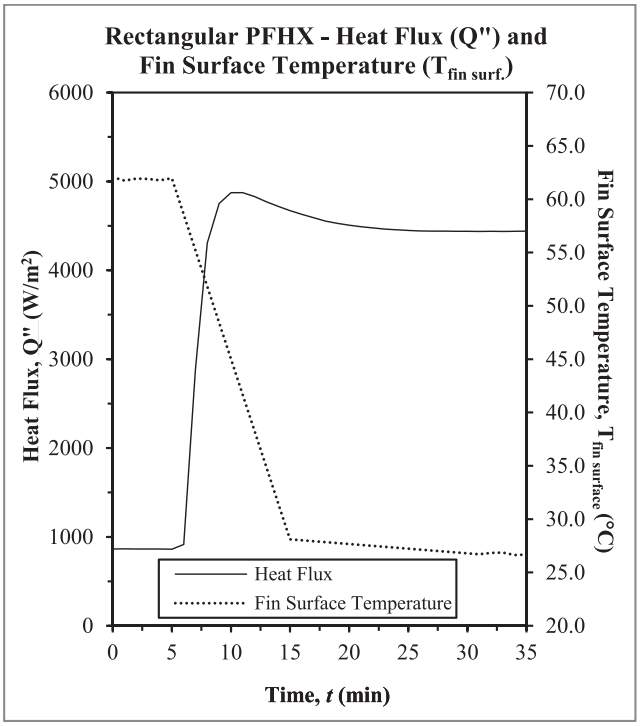

Fig. 4. Plots for heat flux and fin surface temperature for Rectangular PFHX.

deviations of measured parameters, and can be seen in Table 2. Although experiments were carried out in a temperature-controlled facility, a 0.4 % mean uncertainty was noted as room temperature fluctuated to adjust around the set point. Likewise, an average uncertainty of 1.0 % was noted in fin surface temperature measurements as optics from the thermal camera, as well as heat flux from the heater and cooling of the PFHX were affected by fluctuating room temperatures. For pressure drop, a mean uncertainty of 1.1 % can be noted in measured values, which is acceptable as measurements were taken in the wake region (behind the fin). Overall, an average experimental uncertainty of 0.8 % can be noted for all measured parameters.

2.4. Numerical modelling

In the numerical model, heat was supplied to the base of the PFHX based on experimental heat flux results for the rectangular PFHX at each corresponding velocity. A schematic representation of the boundary conditions used for the numerical model is illustrated in Fig. 5. The following assumptions were used in the numerical model: air behaved as an ideal gas (to account for changes in density due to temperature differences); lateral walls on the HX base were adiabatic (no heat losses to surroundings); and the bottom panel consisted only of acrylic as material (no inclusion of calcium silicate insulation to reduce complexity of simulation). No-slip shear conditions were applied to all wall surfaces in the fluid domain. A symmetry boundary was included (at z = 0) in the model due to the symmetric nature of the rectangular PFHX. The resultant fluid domain measured at 62.5 mm x 125 mm in breadth and height, and 350 mm in length.

Experimentally measured velocity, u_x, and corresponding atmospheric temperature, $T_{atm,x}$,were set as inflow boundary conditions. The inlet of the fluid domain was set as a velocity-inlet. Heat flux, Q''_x, recorded during experiment at velocity u_x, was set as heat input. The outlet of the fluid domain was set as a pressure-outlet. The outflow boundary conditions were zero-gauge pressure, $P_{gauge,\ outlet} = 0$, and temperature fixed at the inlet value, $T_{outlet} = T_{inlet}$. Wall roughness and emissivity for acrylic and stainless steel 17-4PH were also accounted for in the numerical model. A turbulent intensity sensitivity study was conducted between 2 % and 20 % to enhance stability, and to compensate for the model's shortened domain size in the wake region by calibrating for fluctuations in pressure drop based on standard deviations of experimental values. For a turbulence intensity of 12 %, standard deviations for numerical results for pressure drop closely matched experimental data over the last 20 % of iterations. Hence, a turbulent intensity of 12 % was used at the inlet and the outlet of the test section.

A Conjugate Heat Transfer (CHT) simulation was set-up to solve the coupled heat transfer and turbulence problem. In terms of turbulence model, a Shear-Stress Transport (SST) k-ω model was chosen to account for compressibility effects and viscous heating. The SST k-ω model can accurately predict both thermal and velocity boundary layers in heat exchanger applications, as reported by Yu et al. [42], Tariq et.al [43] and Wang et al.[44]. For instance, the SST k-ω model adopts the k-ω model in the viscous sub-layer and the k-ε model in regions away from the wall, whereby this is more accurate in simulating wall heat transfer induced by near-wall shears [45]. An important requirement for using the SST k-ω model is to ensure that the dimensionless normal distance from the wall to the first central node of the mesh in the fluid domain (y^+) is less than 1 for accurate calculation of shear stress and heat flux at the wall [46]. Considering air as an ideal gas, for three-dimensional, steady and compressible turbulent flows, the continuity and momentum equations in the cartesian tensor form, and the energy equation are as follows [47]:

Continuity

$$\frac{\partial}{\partial x_i}(\rho u_i) = 0 \tag{1}$$

where, ρ (kg/m^3) is the density, and u_i (m/s) denotes the velocity components.

Momentum

$$\frac{\partial}{\partial x_j}(\rho u_i u_j) = -\frac{\partial p}{\partial x_i} + \frac{\partial}{\partial x_j}\left[\mu\left(\frac{\partial u_i}{\partial x_j} + \frac{\partial u_j}{\partial x_i} - \frac{2}{3}\delta_{ij}\frac{\partial u_l}{\partial x_l}\right)\right] + \frac{\partial}{\partial x_j}\left(-\rho\overline{u_i' u_j'}\right) \tag{2}$$

where, ρ (kg/m^3) is the density, u_i (m/s) denotes the velocity components, p (Pa) is the pressure, μ (Pa·s) is the dynamic viscosity, and $-\rho\overline{u_i' u_j'}$ are Reynolds stresses that close the equation.

Energy

$$\nabla\left[\rho u\left(h + \frac{u^2}{2}\right)\right] = \nabla\left(k_{eff}\Delta T - \sum_j h_j \vec{J}_j + \bar{\bar{\tau}}_{eff}\vec{u}\right) + S_h \tag{3}$$

where, k_{eff} (W/mK) is the effective thermal conductivity, $\vec{J}_j$ is the diffusion of flux species j, S_h is the volumetric heat source, $\bar{\bar{\tau}}_{eff}$ (Pa) is the effective stress tensor, u (m/s) is the velocity magnitude, $\vec{u}$ (m/s) is the overall velocity vector, T (K) is the temperature, and h (J/kg) is the enthalpy.

As previously described, the k-ω SST model accounts for the transport of turbulence shear stress in the definition of turbulent shear viscosity, which gives highly accurate predictions on the onset and amount of flow separation under an adverse pressure gradient [48]. Transport equations for the steady state k-ω SST model can be expressed as [47]:

$$\frac{\partial}{\partial x_i}(\rho k u_i) = \frac{\partial}{\partial x_j}\left(\Gamma_k \frac{\partial k}{\partial x_j}\right) + G_k - Y_k + S_k + G_b \tag{4}$$

$$\frac{\partial}{\partial x_i}(\rho \omega u_i) = \frac{\partial}{\partial x_j}\left(\Gamma_\omega \frac{\partial \omega}{\partial x_j}\right) + G_\omega - Y_\omega + D_\omega + S_\omega + G_{\omega b} \tag{5}$$

where, Γ_k and Γ_ω represent the effective diffusivity of turbulent kinetic energy (k) and dissipation rate (ω), respectively; G_k represents the production of k; G_ω represents the generation of ω; and Y_k and Y_ω represent the dissipation of k and ω due to turbulence. S_k and S_ω are user-defined source terms, D_ω represents the cross-diffusion term and G_b and $G_{\omega b}$ account for buoyancy terms [47]. The effective diffusivities are given by:

$$\Gamma_k = \mu + \left(\frac{\mu_t}{\sigma_k}\right) \tag{6}$$

Table 2
Summary of measured experimental uncertainties.

Velocity, u(m/s)		Pressure Drop, ΔP(Pa)		Heat Flux,Q" (W/m^2)		Fin Surface Temperature,$T_{fin\ surf.}$ (°C)		Atmospheric Temperature, $T_{atm.}$ (°C)	
v	% Uncertainty	ΔP	% Uncertainty	Q"	% Uncertainty	$T_{fin\ surf.}$	% Uncertainty	$T_{atm.}$	% Uncertainty
12	0.4	77	1.2	3970	0.5	34.4	1.5	22.8	0.5
16	0.3	125	0.8	4228	0.1	32.6	1.4	22.8	0.6
20	0.4	189	0.9	4434	0.2	30.8	0.9	22.7	0.4
24	0.4	267	1.0	4558	0.3	29.0	1.0	22.9	0.1
28	0.5	355	1.3	4673	0.5	27.5	0.2	22.8	0.4

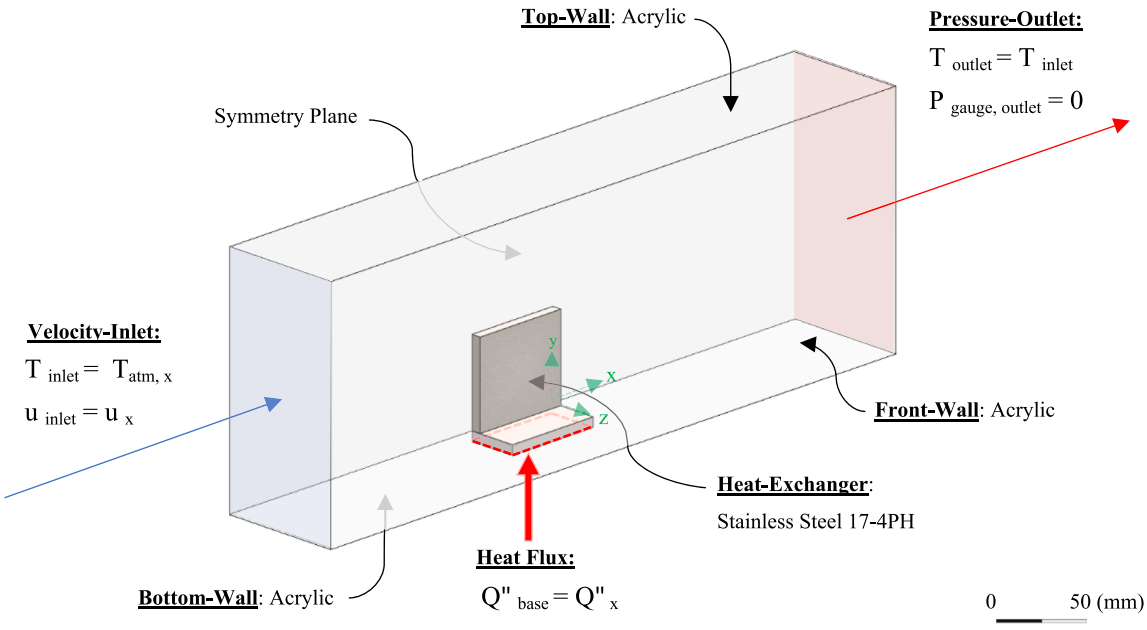

Fig. 5. Boundary conditions imposed to fluid and solid regions (symmetric hypothesis).

$$\Gamma_\omega = \mu + \left(\frac{\mu_t}{\sigma_\omega}\right) \tag{7}$$

where σ_k *and* σ_ω are the turbulent Prandtl numbers for k and ω, respectively; μ (Pa·s) represents the dynamic viscosity; and, μ_t (Pa·s) is the turbulent viscosity.

The k-ω SST model accounts for the transport of the turbulent shear stress which accurately predicts the eddy-viscosity. The k-ω SST models the transport behaviour by introducing a limiter to the formulation of the eddy-viscosity. The turbulent viscosity, μ_t is estimated by:

$$\mu_t = \frac{\rho k}{\omega}\left(\frac{1}{max\left[\frac{1}{\alpha^*}, \frac{SF_2}{\alpha_1 \omega}\right]}\right) \tag{8}$$

where S is the strain rate magnitude, α^* represents damping coefficient, and F_2 is the blending function given by:

$$F_2 = \tanh\left(\phi_2^2\right) \tag{9}$$

$$\phi_2 = max\left[2\frac{\sqrt{k}}{0.09\omega y}, \frac{500\mu}{\rho y^2 \omega}\right] \tag{10}$$

where y [m] is the distance to the next surface.

Further, surface-to-surface (S2S) radiation was used to account for radiation in the three-dimensional system. The energy flux leaving a given surface is composed of directly reflected and emitted energy. The energy leaving from a surface k is given by:

$$q_{out,k} = \varepsilon_k \sigma T_k^4 + (1 - \varepsilon_k) q_{in,k} \tag{11}$$

where, $q_{out,k}$ (W/m^2) is the energy flux leaving the surface, ε_k is the emissivity of the surface, T_k (K) is the surface temperature, σ (W/m^{2}K^4) is the Stefan-Boltzmann constant and $q_{in,k}$ (W/m^2) is the energy flux incident on the surface from the surroundings. A coupled pressure–velocity coupling, with second order spatial discretization for pressure, and second order upwind for density, momentum, turbulent kinetic energy, specific dissipation rate and energy, as well as least-squares cell-based gradient have been used as solution methods. A pseudo-transient simulation was run with residual convergence criteria for velocity, k and ω set at 1e^{-6} and energy at 1e^{-10}.

2.4.1. Grid independence study

Prior to the experiments, mesh sensitivity analysis was performed for each PFHX, as listed in Table 3, at 28 m/s (highest velocity from experimental runs) with an arbitrary heat flux of 5000 W/m^2 and atmospheric temperature of 22.1 °C.

Fin surface temperature and pressure drop were set as observables, whereby they were critical parameters in both experimental and numerical studies. To correctly solve the velocity and thermal boundary layer, it was ensured that $y^+ \leq 1$ for all internal walls within the fluid domain. From the grid independence study, intermediate meshes were chosen as they provided the best trade-offs between accuracy and computational time. Illustrations of meshes for both rectangular and denticle PFHXs are shown in Fig. 6.

2.4.2. Numerical model validation

Numerical simulations were performed on the previously validated mesh of the rectangular PFHX (1.5million cells) by using experimental boundary conditions, as described in Section 2.4. To validate the numerical model, experimental and numerical results of fin surface temperature and pressure drop were compared, as illustrated in Table 4.

Since y^+ is velocity-sensitive and the same mesh which was validated at 28 m/s was used at other velocities, it can be observed that y^+ values decrease as velocity decreases, as evident in Table 4. Fluctuations of y^+ with decreasing velocity improved numerical predictions for both

Table 3
Mesh independence for PFHXs at 28 m/s & 5000 W/m^2.

PFHX	Element Count (x10^6)	Pressure Drop, ΔP (Pa)	Fin Surface Temperature, $T_{fin\ surf.}$ (°C)
Rectangular	0.6	365	30.4
	1.5	364	29.2
	2.4	364	28.9
Denticle	0.7	222	30.6
	1.5	265	31.7
	4.2	257	31.1
NACA 0030	0.8	75	29.5
	1.8	105	29.4
	3.8	110	29.5
Cylindrical	0.3	373	30.7
	1.8	163	30.4
	3.6	162	30.3

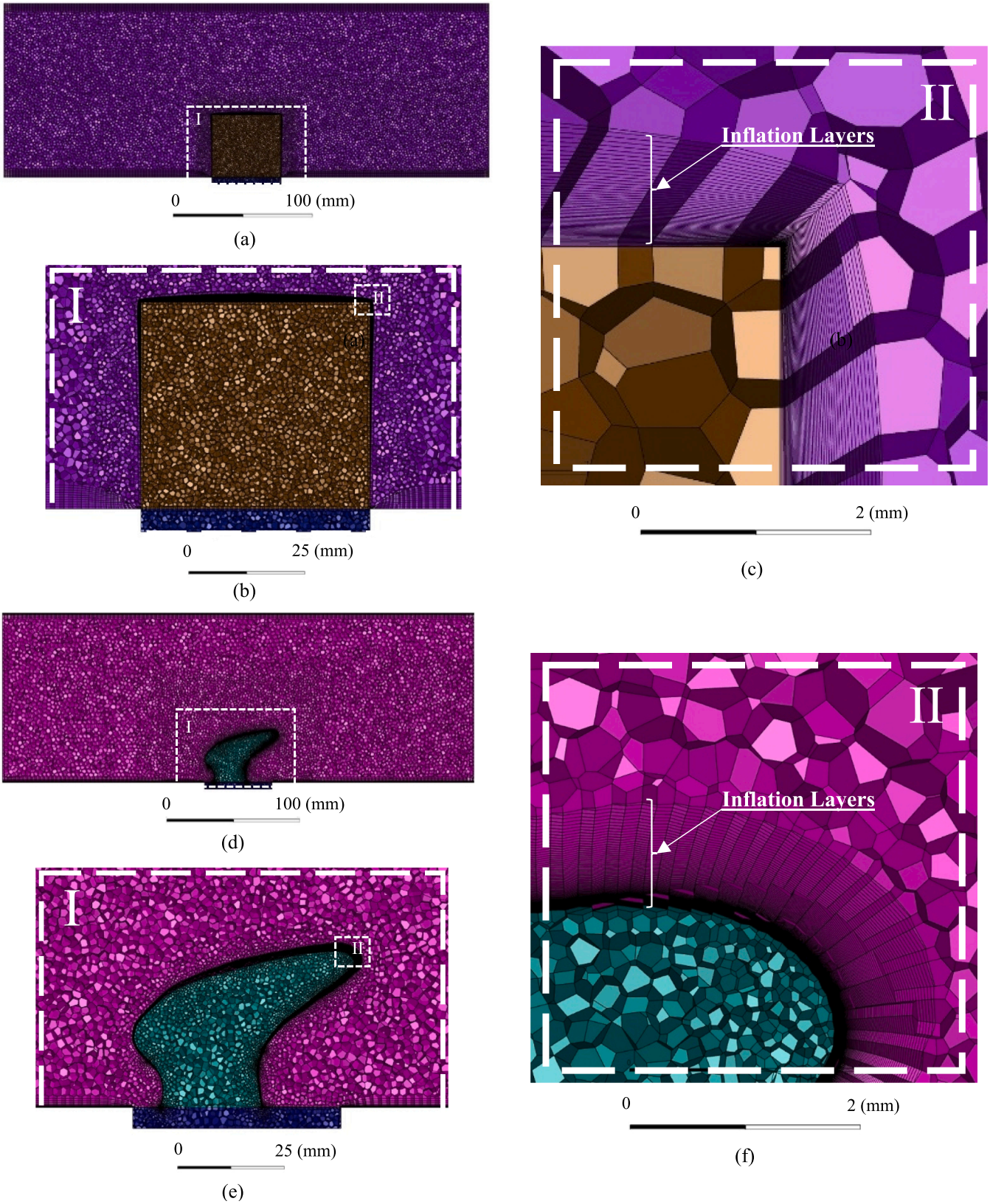

Fig. 6. Illustration of Mesh for PFHXs: (a)Rectangular full domain, (b) Rectangular close-up view on Section I; (c) Rectangular close-up view on Section II; (d) Denticle full domain, (e) Denticle close-up view on Section I; & (f) Denticle close-up view on Section II.

Table 4
Numerical and experimental fin surface temperatures comparison – Rectangular HX.

Inlet velocity u_{inlet} (m/s)	y+	Fin Surface Temperature $T_{Sim.}$(°C)	$T_{Exp.}$(°C)	ΔT_{diff} (°C)	Pressure Drop $\Delta P_{Sim.}$(Pa)	$\Delta P_{Exp.}$(Pa)	ΔP_{diff} (Pa)
12	0.52	34.0	34.4	−0.4	69	77	−7
16	0.66	32.1	32.6	−0.5	122	125	−3
20	0.80	30.7	30.8	−0.1	190	189	1
24	0.94	29.9	29.0	0.9	272	267	5
28	1.07	29.1	27.5	1.6	370	355	15

thermal and velocity boundary layers. In terms of fin surface temperature, a peak difference of 1.6 °C was observed between numerical and experimental results at 28 m/s. For the entire velocity range (12 m/s to 28 m/s), the fin surface temperature difference was less than 2 °C and was within the ± 2 °C accuracy of the thermal camera in the 0 °C-120 °C range. Further, the effect of radiation on simulation results was also investigated. Numerical results demonstrated that heat transfer through radiation accounted for 2 % of the overall heat transfer rate. Hence, to obtain accurate numerical results, the model was validated with the S2S radiation option turned on.

As previously described in Section 2.3.1, two manometers, each with an accuracy of ± 10 Pa, were used during experiments. In terms of pressure drop, between 12 m/s and 24 m/s, pressure differences were less than 10 Pa, falling within the accuracy of the manometers. At 28 m/s, a pressure difference of 15.2 Pa was noted, slightly exceeding the combined error of the measuring instruments. However, this accounted to a deviation of only 4 % compared to the experimental value. Since both average pressure difference (4 %) and fin surface temperature difference (2.4 %) were very low, the numerical simulation was thus validated.

2.5. Performance criteria

By using simulation results, the performances of the HXs were evaluated using the following dimensionless criteria: friction factor for pressure drop evaluations; Nusselt number for thermal performance measurements; and thermal performance factor to evaluate overall performances. This sub-section contains the list of equations used to estimate the performance criteria.

2.5.1. Friction factor, f

Friction factor, more commonly known as Darcy's friction factor, was used to estimate pressure drop across the PFHXs in the test section [49,50]:

$$f = \frac{2D_h \Delta P}{\rho v^2 L} \tag{12}$$

where f is the dimensionless Darcy's friction factor, D_h (m) is the hydraulic diameter of the test section, ΔP (Pa) is the pressure drop between inlet and outlet pitot tubes, ρ (kg/m3) is the fluid density, v (m/s) is the fluid velocity, and L (m) is the length between inlet and outlet pitot tubes.

The hydraulic diameter of the test section, D_h,was calculated using the equation given below [10]:

$$D_h = \frac{2WH}{(H+W)} \tag{13}$$

where W (m) is width and H (m) is the height of the test section.

2.5.2. Reynolds Number, Re

Reynolds number, Re, was calculated using the Equation (14) to characterise the inertial and viscous properties of the moving fluid between the inlet and outlet pitot tubes in the test section [10]:

$$Re = \frac{\rho u D_h}{\mu} \tag{14}$$

where μ (kg/m^{3}s) is the dynamic viscosity of the fluid, u (m/s) is the fluid velocity, D_h (m) is the hydraulic diameter of the test section, and ρ (kg/m3) is the fluid density.

2.5.3. Nusselt Number, Nu

By using heat transfer coefficient values from the numerical results, Nusselt number was calculated to quantify the quality of convective to conductive heat transfer[51]:

$$Nu = \frac{h_c L_f}{k} \tag{15}$$

where h_c is the convective heat transfer coefficient (W/m^{2}K), L_f (m) is the characteristic length of the fin in the flow direction and k is the thermal conductivity of the fluid (W/mK).

2.5.4. Thermal performance factor η

Thermal performance factor, η, is the ratio of enhanced heat transfer to increased friction. This is used to compare the overall relative performances of PFHXs with different geometries [52,53]. The overall thermo-hydraulic performance of the PFHXs were calculated by using Equation (16) [31]:

$$\eta = \frac{\left(\frac{Nu_2}{Nu_1}\right)}{\left(\frac{f_2}{f_1}\right)^{\frac{1}{3}}} \tag{16}$$

where Nu_1 &Nu_2 refer to the Nusselt number for the baseline PFHX and denticle PFHX respectively, and f_1 & f_2 are the Darcy friction factor for baseline PFHX and denticle PFHX respectively.

3. Results and discussion

3.1. Pressure drop analysis

Plots of pressure drop variations for all PFHXs are illustrated in Fig. 7. Overall, the denticle HX created less pressure drop compared to the rectangular fin over the range of simulated Re values. On average, pressure drop across the denticle fin was 19 % less than the rectangular fin. Likewise, a peak decrease in pressure drop of 26 % was noted for the denticle with respect to the rectangular fin at $Re = 22.9 \times 10^4$. Further, an increasing trend was noted between pressure drop plots for denticle and rectangular fin HXs with increasing Re values. For instance, at higher Re, the streamlined form of the denticle fin caused incoming air to attach more to its surface and to converge earlier in the wake region. Dynamic pressure contours along the symmetry plane at z = 0, and xz-plane at y = 22.5 mm,are illustrated in Fig. 8. A diverging flow was noticed across most of the rectangular PFHX surfaces as air reached its leading edges. A low-pressure region was created across the entire lateral face of the PFHX when viewed from the top, as shown in Fig. 8(b). Moderate pressure flows converged back to the rectangular PFHX's surfaces at the

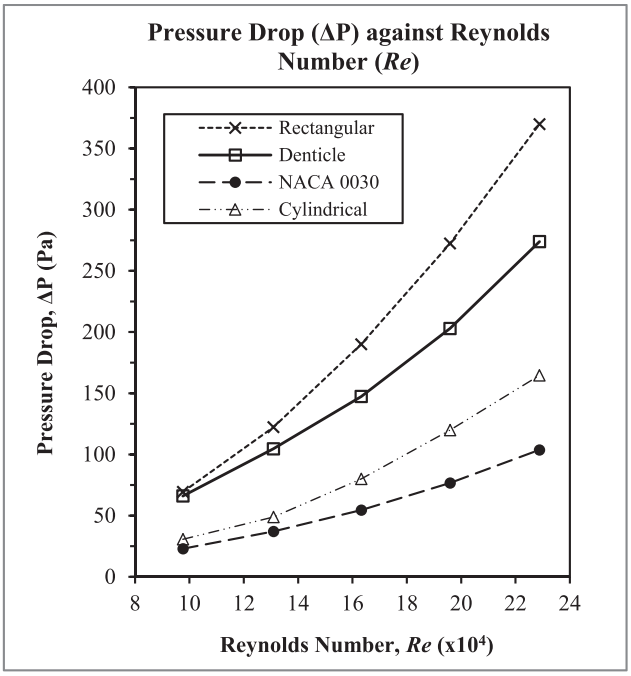

Fig. 7. Plots for pressure drop based on simulation results for all PFHXs.

top end of its trailing edge, as illustrated in Fig. 8(a). The presence of airfoil-like ridges across the geometry of the denticle PFHX caused flow acceleration across the first section of its surface. Further, air attachment to the denticle PFHX's surfaces were enhanced by the streamlined nature of the denticle fin compared to the rectangular fin. By analysing the height and width of the wake, as illustrated in Fig. 8 (c-d), it can be seen how the geometry of the denticle caused air with high dynamic pressure to move downwards and sooner than the rectangular fin in the wake region. For instance, this caused the denticle PFHX to experience less pressure drop compared to the rectangular PFHX.

From Fig. 7, it can be noted that the NACA 0030 and the cylindrical PFHX had better pressure drop performances than the denticle PFHX. As illustrated in Fig. 8 (e-f), the wake for the NACA 0030 fin was narrower and converged more quickly than that of the denticle PFHX. This relative enhancement in the pressure drop performance of the NACA 0030 PFHX might be due to both its reduced frontal area (from Table 1) and its much narrower width in the streamwise direction. Likewise, the cylindrical PFHX had the second-best pressure drop performance relative to the denticle PFHX despite having a similar frontal area. This reduction in pressure drop performance can be explained in terms of shorter length and width of the cylindrical fin in the streamline direction compared to the denticle PFHX. Further, despite being wider than the rectangular PFHX in the streamwise direction, both the NACA 0030 PFHX and cylindrical PFHX had better pressure drop performances due to their smooth leading edges.

3.2. Heat transfer analysis

Plots for normalised fin heat transfer rates for the PFHXs used in this study are illustrated in Fig. 9. Overall, the denticle PFHX had the highest heat transfer rate compared to the other PFHXs, despite having less fin surface area than the rectangular PFHX and the NACA 0030 PFHX. From Fig. 9, it can be observed how the cylindrical PFHX had the worst

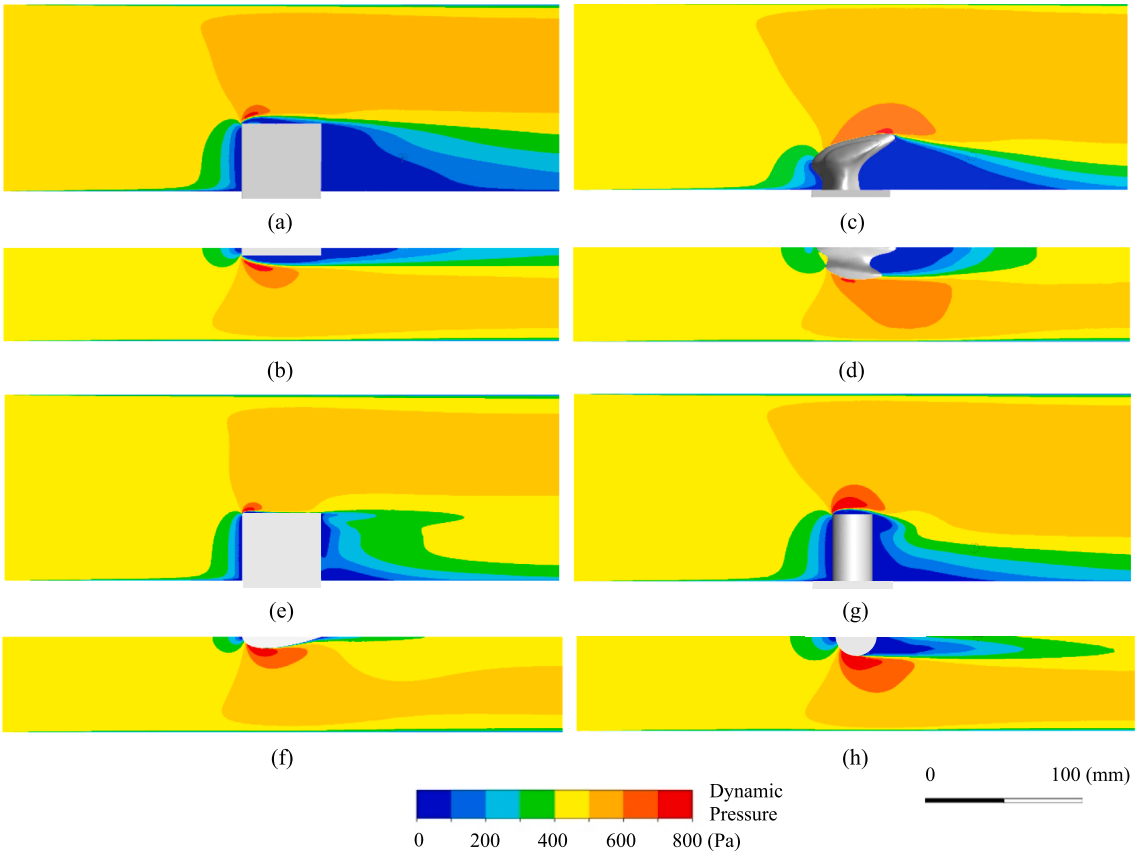

Fig. 8. Dynamic pressure contours for PFHXs at $Re = 22.9x10^4$: (a) Rectangular fin xy-plane at z = 0; (b) Rectangular fin xz-plane at y = 22.5 mm; (c) Denticle fin xy-plane at z = 0; (d) Denticle fin xz-plane at y = 22.5 mm; (e) NACA 0030 fin xy-plane at z = 0; (f) NACA 0030 fin xz-plane at y = 22.5 mm; (g) Cylindrical fin xy-plane at z = 0; & (h) Cylindrical fin xz-plane at y = 22.5 mm.

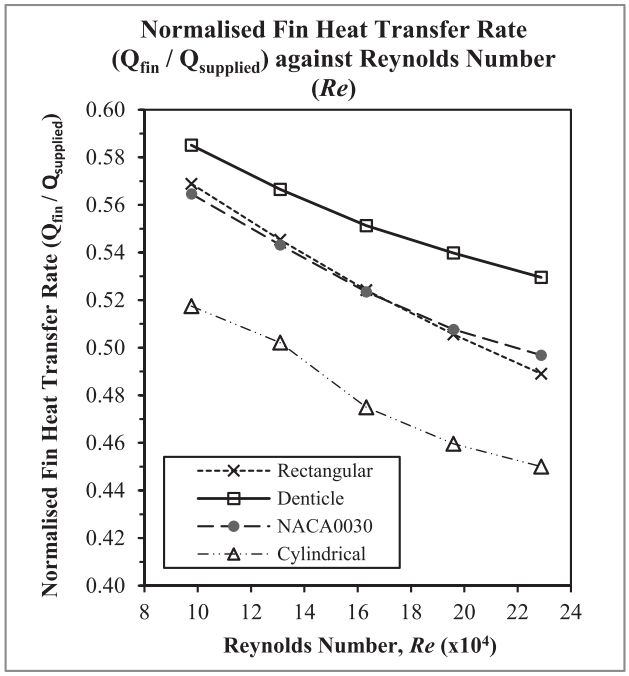

Fig. 9. Plot for normalised fin heat transfer rate from extended fin only for the PFHXs.

normalised heat transfer rate, despite having the same frontal area as the denticle PFHX. The extra surface area on the rectangular PFHX caused the fins to have closely matched normalised heat transfer rates relative to the NACA0030 PFHX. The enhanced heat transfer characteristics of the denticle fin can be attributed to its streamlined shape. The organic shape of the denticle favoured more attachment of incoming air to its surface compared to other PFHXs considered in this study.

Streamlines of turbulent kinetic energy at $Re = 22.9 \times 10^4$ for all PFHXs are illustrated in Fig. 10. For instance, the least turbulence was created along the surfaces of the denticle PFHX, as displayed in Fig. 10 (b). This allowed fluid with higher velocity to contact with the fin's surface, which in turn contributed to enhanced heat extraction from the PFHX's surfaces. Furthermore, the denticle delayed the onset of high turbulence by creating a region of high turbulent kinetic energy only after the fin. Contrastingly, sharp edges on the leading edge of the rectangular fin created two regions of high turbulence along the top and lateral faces, as shown in Fig. 10(a). This caused deflection of air with high velocity away from the fin's surface, which consequently reduced its heat transfer gradient. Similar observations can be made when analysing the flow interaction on the top surface of the cylindrical and NACA 0030 PFHX in Fig. 10(c-d). Likewise, regions of low surface heat transfer coefficient are noted in these same areas, as demonstrated in Fig. 11. For instance, these demonstrate that turbulence created along the surfaces of the fins have a negative impact on their heat transfer performances. Further, the creation of a region of high turbulent kinetic energy near the trailing edge of the NACA 0030 also contributed to deflecting high velocity air away from the fin's surfaces, as illustrated in Fig. 10(c). This might explain its lower heat rejection capabilities, despite being causing less pressure drop than the denticle PFHX. Furthermore, as depicted in Fig. 11 (c), it is evident that the denticle fin had a higher proportion of its frontal and lateral surfaces with regions of high heat transfer coefficients compared to the other fins.

4. Analysis of results

Nusselt number (*Nu*) and friction factor (*f*) were used as performance indicators to characterise the thermal and pressure drop performances of the PFHXs, as illustrated in Fig. 12. From Fig. 12(a), it can be observed that the denticle PFHX has superior heat transfer performance at all *Re* values compared to the other PFHXs. However, this improvement in heat transfer for the denticle occurred at the expense of an increase of friction factor with respect to the NACA 0030 and the cylindrical PFHX, as illustrated in Fig. 12(b). Further, it can be observed that Nusselt number differences increased with increasing *Re* values. For instance, at $Re = 22.9 \times 10^4$, maximum Nusselt number improvements of 16.8 %, 11.5 % and 81.4 % were measured for the denticle PFHX with respect to the rectangular PFHX, the NACA 0030 PFHX and the cylindrical PFHX, respectively. Hence, to account for the combined effects of Nusselt number and friction factor, the thermal performance factor (η) was used to evaluate the efficiency of the denticle PFHX with respect to the other PFHXs, as illustrated in Table 5..

As discussed in Section 2.5, thermal performance factor (η) is the ratio of enhanced heat transfer to increased friction. As *Re* increased from 9.8×10^4 to 22.9×10^4, ratios of Nusselt number for the denticle PFHX were greater than unity and increased with respect to the rectangular PFHX, the NACA 0030 PFHX and the cylindrical PFHX. Accordingly, a ratio of Nusselt number greater than unity indicates that the denticle PFHX is more efficient in terms of heat transfer. Conversely, a friction factor ratio greater than unity demonstrates that the denticle PFHX is less efficient in terms of pressure drop. At all simulated *Re* values, friction factor ratios of more than unity were noted for the denticle PFHX with respect to the NACA 0030 PFHX and cylindrical PFHX. However, friction factor ratios of less than unity were observed at all *Re* values for the denticle PFHX with respect to the rectangular PFHX.

In the context of this study, a thermal performance factor (η) exceeding unity signifies that the denticle PFHX is more efficient than the PFHX being subjected to comparison. From Table 5, it can be observed that at all *Re* values the thermal performance factor of the denticle PFHX is less than that of the NACA 0030 PFHX. For instance, the superior pressure drop performance of the NACA0030 PFHX offsets its inferior thermal performance; therefore, causing it to be more efficient than the denticle PFHX. Contrastingly, the denticle PFHX is more efficient than the cylindrical fin at all *Re* values, as the denticle's enhancements in heat transfer offset its decreases in pressure drop performance. For instance, an average thermal performance factor of 1.42 is noted for the denticle PFHX with respect to the cylindrical PFHX. Further, by having superior thermal and pressure drop performances for the range of simulated *Re* values, the denticle is more efficient than the rectangular PFHX with an average thermal performance factor of 1.21. At $Re = 22.9 \times 10^4$, maximum thermal performance factor improvements were noted for the denticle PFHX relative to the rectangular PFHX, the NACA 0030 PFHX and the cylindrical PFHX, showing the suitability of using the denticle PFHX in high-*Re* applications.

5. Conclusions

In this work, a shark denticle-inspired plate fin heat exchanger was designed for the first time and its performance as a solid-to-air heat exchanger was numerically investigated. An initial experimental study was performed on a baseline rectangular fin to obtain boundary conditions and results to validate a numerical model. The validated numerical model was then used to perform conjugate-heat-transfer simulations on the denticle fin as well as a NACA 0030 fin and a cylindrical fin. Results from the numerical study were then used for analysis of their flow patterns and heat transfer characteristics. The results of the numerical study are summarised as follow:

- Sharp leading edges on the top and/or lateral faces of the rectangular fin, whereby the NACA 0030 fin and cylindrical fin create regions of high turbulent kinetic energy along their faces, which deflect high velocity air away from their surfaces. Contrastingly, the shape of the denticle shifts the onset of high turbulent kinetic energy in its wake region, allowing more effective contact of its surfaces with high velocity air.

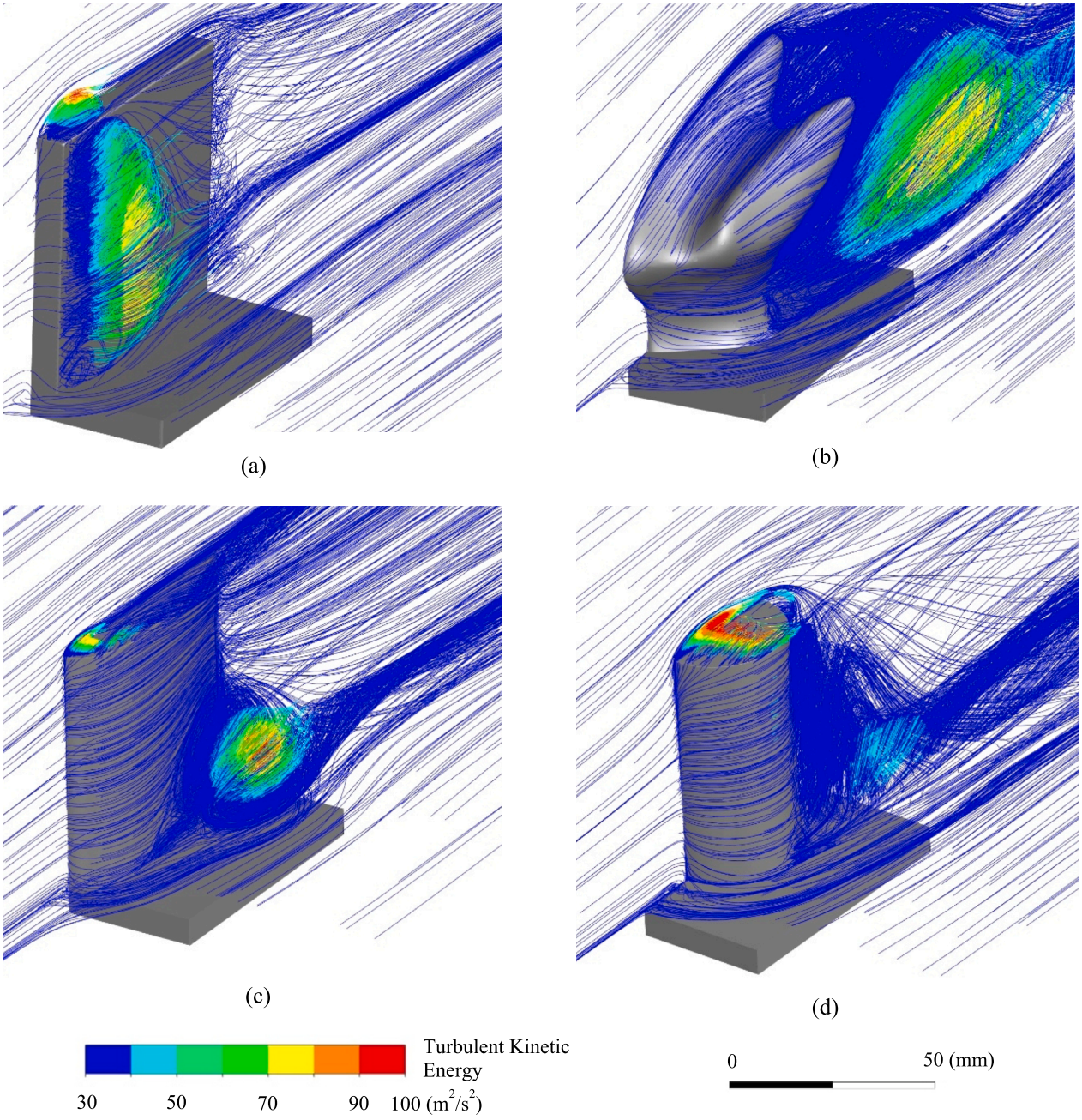

Fig. 10. Streamlines of turbulent kinetic energy at $Re = 22.9x10^4$ for PFHXs: (a) Rectangular fin; (b) Denticle fin HX; (c) Elliptical Fin; & (d) Cylindrical Fin.

- Despite having less surface area than both the rectangular and NACA 0030 plate fin heat exchanger, the denticle had the highest heat transfer rate from its wall surfaces. The streamlined shape of the denticle fin creates less boundary layer flow separation along its surfaces, thereby improving its heat rejection capabilities compared to the other plate fin heat exchangers.
- The effect of the denticle fin shape on pressure drop reduction is high when compared to the rectangular plate fin heat exchanger. An average decrease of 19 % was noted in pressure drop compared to the rectangular fin. Additionally, the denticle fin exhibited increasing pressure reduction characteristics with increasing Reynolds number (*Re*). Further, a peak improvement of 26 % was noted in pressure drop at $Re = 22.9x10^4$ for the denticle fin with respect to the rectangular fin. However, the NACA 0030 fin and the cylindrical fin had significantly better pressure drop performances compared to the denticle fin.
- Average Nusselt number improvements of 13.1 %, 5.4 % and 75.7 % were noted for the denticle fin with respect to the rectangular, the NACA 0030 and cylindrical plate fin heat exchanger for the range of tested Reynolds number.
- At $Re = 22.9x10^4$, a peak thermal performance factor (η) of 1.29 and 1.53 were noted for the denticle fin with respect to the rectangular fin and the cylindrical fin.
- Overall, the denticle fin is more efficient than both rectangular fin and cylindrical fin, with a thermal performance factor of greater than unity for the range of tested Reynolds number. However, the denticle plate fin heat exchanger is less efficient than the NACA 0030 one for the range of simulated Reynolds number.

This current study has shown the potential of using a shark denticle-inspired fin geometry as compared to commonly used conventional fin geometries for plate fin heat exchangers. Further, this study has

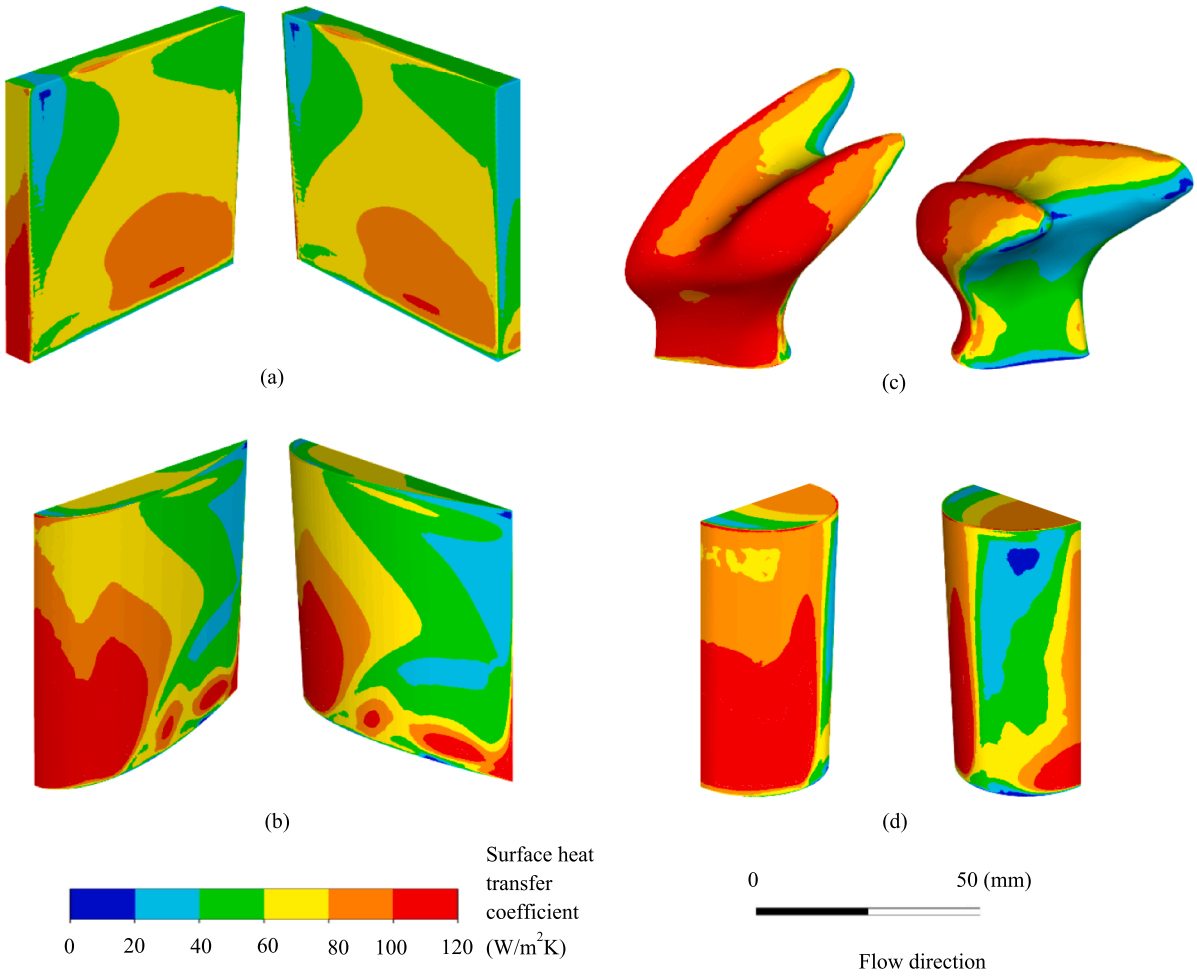

Fig. 11. Surface heat transfer coefficient plots at $Re = 22.9x10^4$ for PFHXs: (a) Rectangular fin; (b) Denticle fin HX; (c) Elliptical Fin; & (d) Cylindrical Fin.

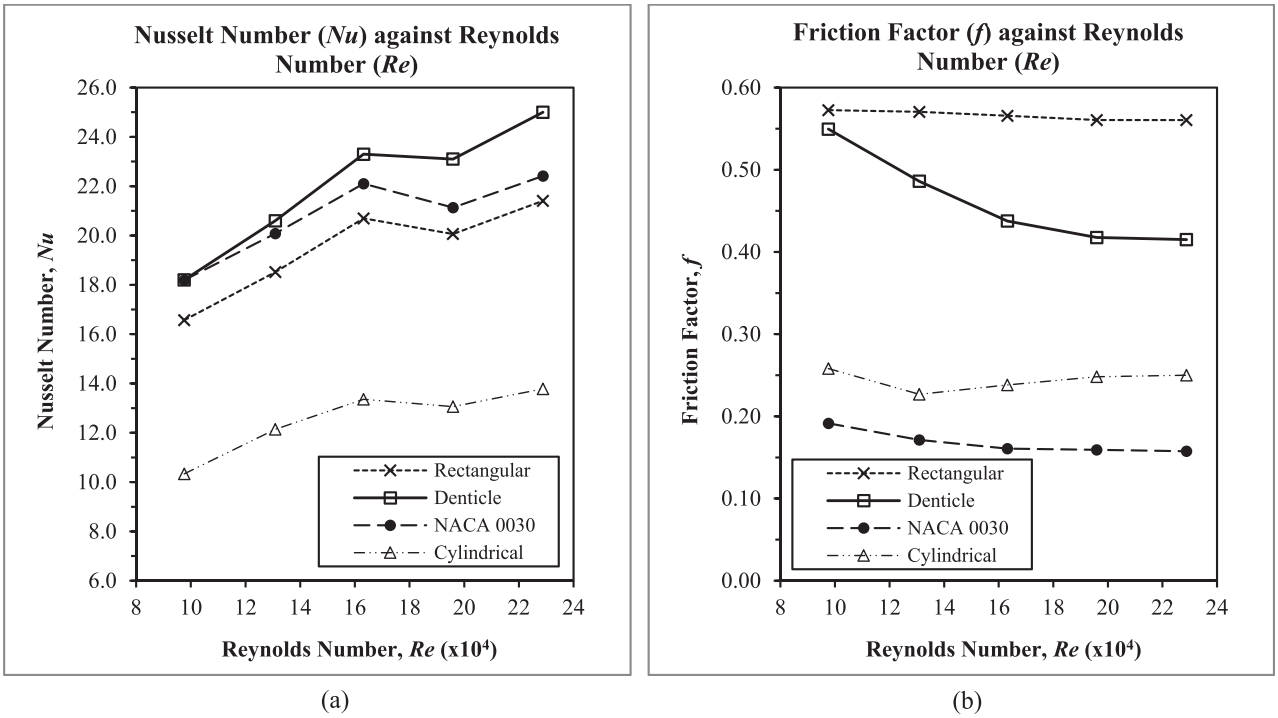

Fig. 12. Plots of performance indicators for PFHXs: (a) Nusselt number; &(b) Friction factor.

Table 5
Thermal Performance Factor for the denticle fin HX at different Reynolds number.

Re (x10^4)	η Denticle w.r.t. Rect.	η Denticle w.r.t. NACA 0030	η Denticle w.r.t. Cylind.
9.8	1.11	0.70	1.37
13.1	1.17	0.72	1.32
16.3	1.23	0.76	1.42
19.6	1.27	0.79	1.49
22.9	1.29	0.81	1.53

provided an outlook on the process to evaluate the efficiency of a nature inspired geometry by using biomimicry and a combination of numerical and experimental methods. Results have shown the possibility of using a shark denticle plate fin heat exchanger for its enhanced heat transfer capabilities for $9.8x10^4 < Re \leq 22.9x10^4$. Additionally, flow visualisations have demonstrated promising results in terms of boundary layer attachment to the surface of the denticle plate fin heat exchanger compared to the streamlined NACA 0030. These results show exciting prospects for the use of the shark denticles in arrays and/or as surface textures for the creation of more compact heat exchangers. To conclude, the denticle fin had the highest heat rejection capabilities compared to the other plate fin heat exchangers used in this study. Hence, by using biomimicry, nature can be used as a source of inspiration to design novel fin geometries to create more efficient plate fin heat exchangers.

Funding:

This study was supported by Edith Cowan University (ECU) under Grant G1004423.

CRediT authorship contribution statement

Aakash S. Hurry: Conceptualization, Investigation, Methodology, Writing – original draft, Visualization. **Ana Vafadar:** Supervision, Project administration. **Kevin Hayward:** Writing – review & editing, Supervision. **Ferdinando Guzzomi:** Writing – review & editing, Supervision. **Kanishk Rauthan:** Writing – review & editing.

Declaration of competing interest

The authors declare that they have no known competing financial interests or personal relationships that could have appeared to influence the work reported in this paper.

Data availability

No data was used for the research described in the article.

Acknowledgement

The first author would like to thank ECU for the HDR Scholarship in Additive Manufacturing. Additionally, the first author would like to Dr. Michael Stein for providing writing and editing support for this article, and to thank Mr Adrian Davies and Mr Yatt Yap for their technical assistance.

References

[1] I. Kaur, P. Singh, State-of-the-art in heat exchanger additive manufacturing, International Journal of Heat and Mass Transfer 178 (2021/10/01/ 2021) 121600, https://doi.org/10.1016/j.ijheatmasstransfer.2021.121600.
[2] T.L. Bergman, A.S. Lavine, F.P. Incropera, D.P. DeWitt, Fundamentals of Heat and Mass Transfer, 8th Edition, Wiley, New York, UNITED STATES, 2016.
[3] K. Thulukkanam, Heat exchanger design handbook, CRC Press, 2013.
[4] B. Zohuri, *Compact heat exchangers : selection, application, design and evaluation*, Cham: Springer, 2017. [Online]. Available: http://public.ebookcentral.proquest.com/choice/publicfullrecord.aspx?p=4694130.
[5] R.L. Webb, Air-Side Heat Transfer in Finned Tube Heat Exchangers, Heat Transfer Engineering 1 (3) (1980/01/01 1980,) 33–49, https://doi.org/10.1080/01457638008939561.
[6] A.S. Sabau, et al., Design, additive manufacturing, and performance of heat exchanger with a novel flow-path architecture, Applied Thermal Engineering 180 (2020/11/05/ 2020) 115775, https://doi.org/10.1016/j.applthermaleng.2020.115775.
[7] A.A. Gholami, M.A. Wahid, H.A. Mohammed, Heat transfer enhancement and pressure drop for fin-and-tube compact heat exchangers with wavy rectangular winglet-type vortex generators, International Communications in Heat and Mass Transfer 54 (2014/05/01/ 2014) 132–140, https://doi.org/10.1016/j.icheatmasstransfer.2014.02.016.
[8] G. Wang, et al., Experimental and numerical investigation of fractal-tree-like heat exchanger manufactured by 3D printing, Chemical Engineering Science 195 (2019/02/23/ 2019) 250–261, https://doi.org/10.1016/j.ces.2018.07.021.
[9] A. Vafadar, F. Guzzomi, and K. Hayward, "Experimental Investigation and Comparison of the Thermal Performance of Additively and Conventionally Manufactured Heat Exchangers," *Metals,* vol. 11, no. 4, p. 574, 2021. [Online]. Available: https://www.mdpi.com/2075-4701/11/4/574.
[10] K. Rauthan, F. Guzzomi, A. Vafadar, K. Hayward, and A. Hurry, "Experimental Investigation of Pressure Drop Performance of Smooth and Dimpled Single Plate-Fin Heat Exchangers," *Metals,* vol. 11, no. 11, p. 1757, 2021. [Online]. Available: https://www.mdpi.com/2075-4701/11/11/1757.
[11] D. Calamas, J. Baker, Tree-like branching fins: Performance and natural convective heat transfer behavior, International Journal of Heat and Mass Transfer 62 (2013/07/01/ 2013) 350–361, https://doi.org/10.1016/j.ijheatmasstransfer.2012.12.050.
[12] N. Sahiti, F. Durst, A. Dewan, Heat transfer enhancement by pin elements, International Journal of Heat and Mass Transfer 48 (23) (2005/11/01/ 2005) 4738–4747, https://doi.org/10.1016/j.ijheatmasstransfer.2005.07.001.
[13] A.I. Bashir, M. Everts, R. Bennacer, J.P. Meyer, Single-phase forced convection heat transfer and pressure drop in circular tubes in the laminar and transitional flow regimes, Experimental Thermal and Fluid Science 109 (2019/12/01/ 2019) 109891, https://doi.org/10.1016/j.expthermflusci.2019.109891.
[14] M.A. Arie, A.H. Shooshtari, M.M. Ohadi, Experimental characterization of an additively manufactured heat exchanger for dry cooling of power plants, Applied Thermal Engineering 129 (2018/01/25/ 2018) 187–198, https://doi.org/10.1016/j.applthermaleng.2017.09.140.
[15] D. Jafari, W.W. Wits, The utilization of selective laser melting technology on heat transfer devices for thermal energy conversion applications: A review, Renewable and Sustainable Energy Reviews 91 (2018/08/01/ 2018) 420–442, https://doi.org/10.1016/j.rser.2018.03.109.
[16] Y. Cormier, P. Dupuis, A. Farjam, A. Corbeil, B. Jodoin, Additive manufacturing of pyramidal pin fins: Height and fin density effects under forced convection, International Journal of Heat and Mass Transfer 75 (2014/08/01/ 2014) 235–244, https://doi.org/10.1016/j.ijheatmasstransfer.2014.03.053.
[17] P. Dupuis, Y. Cormier, M. Fenech, B. Jodoin, Heat transfer and flow structure characterization for pin fins produced by cold spray additive manufacturing, International Journal of Heat and Mass Transfer 98 (2016/07/01/ 2016) 650–661, https://doi.org/10.1016/j.ijheatmasstransfer.2016.03.069.
[18] K.L. Kirsch, K.A. Thole, Pressure loss and heat transfer performance for additively and conventionally manufactured pin fin arrays, International Journal of Heat and Mass Transfer 108 (2017/05/01/ 2017) 2502–2513, https://doi.org/10.1016/j.ijheatmasstransfer.2017.01.095.
[19] H. Zhao, Z. Liu, C. Zhang, N. Guan, H. Zhao, Pressure drop and friction factor of a rectangular channel with staggered mini pin fins of different shapes, Experimental Thermal and Fluid Science 71 (2016/02/01/ 2016) 57–69, https://doi.org/10.1016/j.expthermflusci.2015.10.010.
[20] O.P. Arsenyeva, L.L. Tovazhnyansky, P.O. Kapustenko, G.L. Khavin, Optimal design of plate-and-frame heat exchangers for efficient heat recovery in process industries, Energy 36 (8) (2011/08/01/ 2011) 4588–4598, https://doi.org/10.1016/j.energy.2011.03.022.
[21] Z. Huang, Y. Hwang, R. Radermacher, Review of nature-inspired heat exchanger technology, International Journal of Refrigeration 78 (2017/06/01/ 2017) 1–17, https://doi.org/10.1016/j.ijrefrig.2017.03.006.
[22] N.-T. Le, J. Warschat, T. Farrenkopf, in: "an Early-Biologisation Process to Improve the Acceptance of Biomimetics in Organizations," in *Advanced Computational Methods for Knowledge Engineering*, Springer International Publishing, 2018// 2018: , pp. 175–183.
[23] J. Knippers, T. Speck, Design and construction principles in nature and architecture, Bioinspiration & Biomimetics 7 (1) (2012/02/16 2012) 015002, https://doi.org/10.1088/1748-3182/7/1/015002.
[24] S. Cui, Y. Hu, Z. Huang, C. Ma, L. Yu, X. Hu, Cooling performance of bio-mimic perspiration by temperature-sensitive hydrogel, International Journal of Thermal Sciences 79 (2014/05/01/ 2014) 276–282, https://doi.org/10.1016/j.ijthermalsci.2014.01.015.
[25] X.-Q. Wang, P. Xu, A.S. Mujumdar, C. Yap, Flow and thermal characteristics of offset branching network, International Journal of Thermal Sciences 49 (2) (2010/02/01/ 2010) 272–280, https://doi.org/10.1016/j.ijthermalsci.2009.07.019.
[26] D. Bacellar, V. Aute, Z. Huang, and R. Radermacher, "Novel airside heat transfer surface designs using an integrated multi-scale analysis with topology and shape optimization," 2016.
[27] B. Gürel, et al., Investigation on flow and heat transfer of compact brazed plate heat exchanger with lung pattern, Applied Thermal Engineering 175 (2020/07/05/ 2020) 115309, https://doi.org/10.1016/j.applthermaleng.2020.115309.
[28] N. Geographic. "Can the Ocean's Fastest Shark Outswim Our Appetite for It?" National Geographic https://www.nationalgeographic.com/magazine/2017/08/shortfin-mako-fastest-shark-ocean/#:~:text=Shortfin%20makos%20are%20the%

20fastest,sport%20fishermen%20love%20their%20power. (accessed 18 October, 2020).
[29] L. Wen, J.C. Weaver, G.V. Lauder, "Biomimetic shark skin: design, fabrication and hydrodynamic function," (in eng), J Exp Biol 217 (Pt 10) (2014) 1656–1666, https://doi.org/10.1242/jeb.097097.
[30] K. Rauthan, F. Guzzomi, A. Vafadar, K. Hayward, and A. Hurry, "Experimental Investigation of Pressure Drop Performance of Smooth and Dimpled Single Plate-Fin Heat Exchangers," *Metals*, vol. 11, no. 11, 10.3390/met11111757.
[31] P. Eiamsa-ard, N. Piriyarungroj, C. Thianpong, and S. Eiamsa-ard, "A Case Study on Thermal Performance Assessment of a Heat Exchanger Tube Equipped with Regularly-Spaced Twistes Tapes as Swirl Generators," *Case Studies in Thermal Engineering,* pp. 86-102, 2014.
[32] A. Vafadar, F. Guzzomi, A. Rassau, K. Hayward, Advances in Metal Additive Manufacturing: A Review of Common Processes, Industrial Applications, and Current Challenges, Applied Sciences 11 (3) (2021) pp, https://doi.org/10.3390/app11031213.
[33] T. Ltd. "Bench-Top Wind Tunnel." TecQuipment. https://www.tecquipment.com/bench-top-wind-tunnel (accessed 17 January, 2022).
[34] T. F. LLC. "FLIR IR Windows- Infrared Camera window with PIRma- Lock." https://www.flir.com.au/products/ir-windows/?model=19252-100 (accessed).
[35] Sauermann. "KIMO VT110 Hotwire thermo-anemometer." https://sauermanngroup.com/en-AU/measuring-instruments/portable-instruments/anemometers/vt-110-vt-115 (accessed 18 January, 2022).
[36] F. S. Extech. "HD755: Differential Pressure Manometer (0.5psi)." http://www.extech.com/products/HD755 (accessed Jan 21, 2022).
[37] O. E. Inc. "4-Channel RTD input DAQ Module with USB or Ethernet Interface." https://www.omega.com/en-us/data-acquisition/data-acquisition-modules/p/PT-104A-DAQ-Module (accessed).
[38] H. T. Sensors. "FHF04SC Heat Flux Sensor - Self-calibrating foil heat flux sensor with thermal spreaders and heater." https://www.hukseflux.com/products/heat-flux-sensors/heat-flux-meters/fhf04sc-heat-flux-sensor (accessed).
[39] H. T. Sensors. "Li-19 Datalogger." https://www.hukseflux.com/products/heat-flux-sensors/heat-flux-sensors/li19-datalogger (accessed 02 February, 2022).
[40] TEquipment. "FLIR T200 Thermal Imaging Infrared Camera." https://www.tequipment.net/FlirT200.html#description (accessed).
[41] J. Taylor, *Introduction to error analysis, the study of uncertainties in physical measurements*. 1997.
[42] B. Yu, et al., A bioinspired programmable Self-Organization approach for designing additively manufactured heat sinks, Energy Conversion and Management 286 (2023/06/15/ 2023) 116996, https://doi.org/10.1016/j.enconman.2023.116996.
[43] A. Tariq, K. Altaf, S.W. Ahmad, G. Hussain, T.A.H. Ratlamwala, Comparative numerical and experimental analysis of thermal and hydraulic performance of improved plate fin heat sinks, Applied Thermal Engineering 182 (2021/01/05/ 2021) 115949, https://doi.org/10.1016/j.applthermaleng.2020.115949.
[44] J. Wang, X.-P. Yan, B.J. Boersma, M.-J. Lu, X. Liu, Numerical investigation on the Thermal-hydraulic performance of the modified channel supercritical CO2 printed circuit heat exchanger, Applied Thermal Engineering 221 (2023/02/25/ 2023) 119678, https://doi.org/10.1016/j.applthermaleng.2022.119678.
[45] M. Mieczkowski, P. Furmański, P. Łapka, Optimization of a microchannel heat sink using entropy minimization and genetic aggregation algorithm, Applied Thermal Engineering 191 (2021/06/05/ 2021) 116840, https://doi.org/10.1016/j.applthermaleng.2021.116840.
[46] A. Rebassa, I. Rahbari, J. Paulson, G. Paniagua, Aerothermal characterization of finned surfaces in high-speed flows, Applied Thermal Engineering 227 (2023/06/05/ 2023) 120331, https://doi.org/10.1016/j.applthermaleng.2023.120331.
[47] *Ansys Fluent Theory Guide,* R. 2023R1, 2023.
[48] J. Wu, J. Xiao, Numerical study of crossed airfoil fins in a printed circuit heat exchanger, Applied Thermal Engineering 230 (2023/07/25/ 2023) 120646, https://doi.org/10.1016/j.applthermaleng.2023.120646.
[49] G.B. Barker, The engineer's guide to plant layout and piping design for the Oil and Gas Industries, Gulf Professional Publishing, 2017.
[50] B. Sahin, I. Ates, E. Manay, A. Bayrakceken, C. Celik, Optimization of design parameters for heat transfer and friction factor in a heat sink with hollow trapezoidal baffles, Applied Thermal Engineering 154 (2019/05/25/ 2019,) 76–86, https://doi.org/10.1016/j.applthermaleng.2019.03.056.
[51] H. Herwig, What Exactly is the Nusselt Number in Convective Heat Transfer Problems and are There Alternatives? Entropy 18 (5) (2016) 1–15.
[52] A. Kumar, M. Kumar, S. Chamoli, Comparative study for thermal-hydraulic performance of circular tube with inserts, Alexandria Engineering Journal 55 (1) (2016/03/01/ 2016) 343–349, https://doi.org/10.1016/j.aej.2015.12.013.
[53] G. Xie, B. Sundén, W. Zhang, Comparisons of Pins/Dimples/Protrusions Cooling Concepts for a Turbine Blade Tip-Wall at High Reynolds Numbers, Journal of Heat Transfer 133 (6) (2011) pp, https://doi.org/10.1115/1.4003558.
[54] A.S. Hurry, K. Hayward, F. Guzzomi, K. Rauthan, A. Vafadar, Thermo-hydraulic performance evaluation of a NACA 63-015 heat exchanger with shark denticles as surface textures, International Journal of Heat and Mass Transfer 216 (2023) 124591, https://doi.org/10.1016/j.ijheatmasstransfer.2023.124591.